

We are IntechOpen, the world's leading publisher of Open Access books Built by scientists, for scientists

4,800

Open access books available

122,000

International authors and editors

135M

Downloads

Our authors are among the

154

Countries delivered to

TOP 1%

most cited scientists

12.2%

Contributors from top 500 universities



WEB OF SCIENCE™

Selection of our books indexed in the Book Citation Index
in Web of Science™ Core Collection (BKCI)

Interested in publishing with us?
Contact book.department@intechopen.com

Numbers displayed above are based on latest data collected.

For more information visit www.intechopen.com



Micro/Nano Hierarchical Super-Lyophobic Surfaces Against Gallium-Based Liquid Metal Alloy

Daeyoung Kim and Jeong-Bong Lee

Additional information is available at the end of the chapter

<http://dx.doi.org/10.5772/60984>

Abstract

Against a gallium-based liquid metal alloy, we report super-lyophobic surfaces that have micro/nano hierarchical structures made of polydimethylsiloxane (PDMS) and carbon nanotube (CNT) materials. The surface oxidation of the liquid metal is a challenging problem to be utilized for various applications, as it wets most surfaces. However, the micro/nano hierarchical structures of a fabricated-PDMS micro pillar array with dual-scale surface texturing and a grown-CNT surface enable one to minimize a contact area between the liquid metal droplet and the surface. Due to the low contact area, a large static contact angle and a low contact angle hysteresis are achieved, indicating super-lyophobic surfaces. Based on these super-lyophobic surfaces, the gallium-based liquid metal alloy can be more widely utilized for undeveloped applications that rely on the liquid metal's mobility.

Keywords: Gallium-based liquid metal alloy, super-lyophobic, micro/nano hierarchical, contact angle, CNT, PDMS

1. Introduction

Gallium-based liquid metal alloy is a non-toxic liquid metal at room temperature. Recently, it has been of interest as the gallium-based liquid metal shows higher thermal and electrical conductivities, and lower vacuum pressure [1] compared to a toxic liquid metal, such as mercury. Based on these favorable material properties, it has been utilized for various applications including micro-cooling [2], electrical interconnector [3], 3D printing [4], tunable frequency antennas [5-11], metamaterials [12, 13], and electrodes [14-18]. However, most of

these applications operate on the deformability of the liquid metal, not on the mobility. This is because it has a very challenging problem that the liquid metal alloy is easily oxidized when it is exposed to ambient air environment. Once it is oxidized, the surface becomes viscous and it makes the liquid metal wet on the surfaces [19]. Thus, there are two ways to utilize the oxidized gallium-based liquid metal alloy: 1) modifying or removing the oxidized surface of the liquid metal and 2) creating the non-wettable channel surface.

There have been a few studies to modify or remove the oxidized surface of the liquid metal. Zrnick and Swatik found that it was possible to remove the oxidized surface of gallium-based liquid metal by treating the surface with diluted hydrochloric acid (HCl) [20]. We also demonstrated that the HCl vapor even can modify the wettable $\text{Ga}_2\text{O}_3/\text{Ga}_2\text{O}$ to non-wettable $\text{GaCl}_3/\text{InCl}_3$ [21]. Based on this method, the oxidized gallium-based liquid metal can be controllable in the microfluidic channels composed of a gas-permeable PDMS [22]. Sivan et al. reported that the liquid metal surface can be simply coated with nano-particles of insulators (including Teflon and silica) and semiconductors (including WO_3 , TiO_2 , MoO_3 , In_2O_3 , and carbon nanotubes) [23]. Then, this liquid metal marble can also be non-wettable by covering the oxidized surface. We also reported that the oxidized surface can be covered with ferromagnetic micro-particles and it can be manipulated with an applied magnetic field [24]. Khan et al. also investigated that the oxidized surface of the liquid metal in the presence of electrolyte can be removed by applying a reductive potential [25].

Alternatively, if there is any surface where the oxidized liquid metal moves without any wetting problem, it may enable one to utilize the liquid metal for new applications that rely on constant and reliable motion of liquid metal. In order to utilize liquid metal's mobility, the surface should be non-wetting and super-lyophobic. The methods of making these surfaces can be analogous to those of creating the well-known super-hydrophobic surfaces.

Over the past decades, super-hydrophobic surfaces have been tremendously investigated due to its wide applicability for self-cleaning [26-28] and anti-icing effect [29, 30]. Conventionally, there are two distinctive ways to engineer the surface to be super-hydrophobic. One way is to make a rough surface to reduce the contact area between the liquid and the solid. The other way is to coat the surface with low surface energy materials such as a fluorocarbon polymer. From nature, one can find water-repelling surfaces such as shark scales and lotus leaves. Those surfaces have one thing in common—that they have micro/nano hierarchical structures to realize the rough surface [31]. This approach can also be applied to the oxidized liquid metal. Thus, the contact area between the liquid metal and the surface can be as small as possible, resulting in the super-lyophobic surface against the oxidized gallium-based liquid metal alloy.

In this chapter, the realization of super-lyophobic surfaces against gallium-based liquid metal alloy, micro/nano hierarchical structure-based surfaces using different materials such as polydimethylsiloxane (PDMS) and carbon nanotube (CNT) are discussed. Wetting phenomena such as lyophobic/lyophilic concepts and wetting models such as Cassie and Wenzel states are described. As demonstrations of super-lyophobic surfaces based on micro/nano hierarchical structure, the lyophobicity of PDMS micro pillar array with surface texturing is characterized by measuring static and dynamic contact angles and compared with those of the PDMS micro pillar and ridge arrays without any surface texturing. In addition, the lyophobicity of CNT on

PDMS is characterized by measuring static and dynamic contact angles, as well as bouncing and rolling experiments under mechanical deformation.

2. Theory

Lyophobic/lyophilic is defined as a physical property of a molecule that is repelled from or attracted to a mass of liquid. Therefore, the term 'lyophobic or lyophilic' needs to be used to indicate a target liquid except when they are 'hydrophobic/hydrophilic' or 'oleophobic/oleophilic', implying that the target liquid is water or oil, respectively. Therefore, 'lyophobic/lyophilic' is a superordinate concept to 'hydrophobic/hydrophilic' and 'oleophobic/oleophilic'.

In order to characterize lyophobicity, the static and dynamic contact angles are important parameters. The static contact angles can be measured by using a goniometer that can capture the profile of a liquid droplet on a solid substrate. The static contact angle depends on the surface tensions of liquid (liquid/gas interfacial energy), solid (solid/gas interfacial energy), and liquid/solid interactions. As shown in Fig. 1a, the static contact angle is defined as an angle formed by the intersection of the liquid-solid interface and the liquid-gas interface. Generally, when the contact angle is smaller than 90° the solid surface is considered to be 'lyophilic', which means wetting of the surface is favorable. When the contact angle is larger than 90° the solid surface is considered 'lyophobic', which indicates the liquid minimizes its contact on the surface and form a compact liquid droplet. In addition, when the contact angle is greater than 150°, the solid surface is considered to be 'super-lyophobic'.

For dynamic contact angle measurements, the volume of liquid was increased or decreased until the droplet had a maximum or minimum contact angle without changing the surface area between the liquid and the solid substrate while the side view of a droplet was recorded. Each of maximum and minimum contact angles is the advancing and receding contact angle, respectively; and the advancing and receding contact angles were obtained from the frame of the recorded movie just before the contact line is changed. The difference between the advancing angle and the receding angle is the contact angle hysteresis. When the advancing and receding contact angle of liquid on a solid substrate are close to each other (lower contact angle hysteresis), it indicates the substrate is lyophobic to the liquid.

Theoretically, as shown in Fig. 1a, Thomas Young described in 1805 the contact angle of a liquid droplet on an ideal solid substrate[32]. It is defined by the mechanical equilibrium of surface tensions of three interfaces under the droplet:

$$\cos\theta = \frac{\gamma_{SG} - \gamma_{SL}}{\gamma_{LG}} \quad (1)$$

where θ is the contact angle, and γ_{SG} , γ_{SL} , and γ_{LG} are surface tension of solid-gas, solid-liquid, and liquid-gas interfaces, respectively. Equation (1) is usually referred as Young's equation.

Since Young's equation only works with a flat homogeneous surface, the other expanded approaches are needed to describe contact angle of a droplet on rough and heterogeneous surfaces: Wenzel model [33] and Cassie model [34].

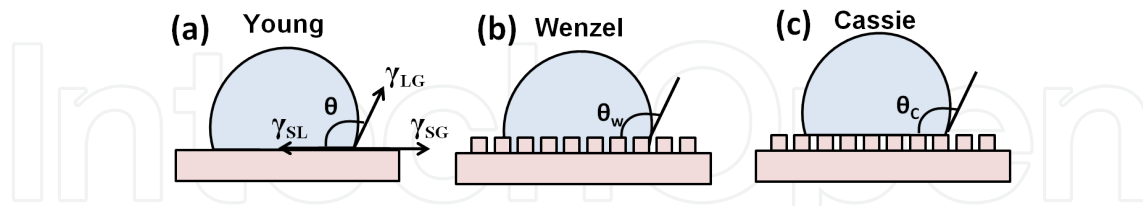


Figure 1. Schematics of different wetting regimes: (a) Young's model, (b) Wenzel model, and (c) Cassie model.

As shown in Fig. 1b, when a liquid can fully wet the surface texture, the thermodynamic equilibrium contact angle of a liquid droplet is described by the Wenzel model [33] as the following equation:

$$\cos \theta_w = r \cos \theta \quad (2)$$

where θ_w is the apparent contact angle of the Wenzel model, θ refers to Young's contact angle, and r is a roughness factor, which is defined as the ratio of an actual area of a rough surface to the flat, projected area. Droplets in this fully wetted Wenzel state typically display very high hysteresis because the contact line of the droplets becomes severely pinned on surface asperities.

On the other hand, when a liquid cannot penetrate into the surface texture, the droplet forms a highly non-wetting regime known as a Cassie state (Fig. 1c). As the surface texture entraps myriads of air pockets underneath the droplet, it can have low adhesive force. Therefore, the droplet in the Cassie state displays a very high contact angle, as well as a low hysteresis, resulting in easy rolling off of a droplet. If f_s is the fraction of the solid in contact with the liquid, the Cassie equation can be represented by Equation (3) [34].

$$\cos \theta_c = f_s (1 + \cos \theta) - 1 \quad (3)$$

Therefore, in order to achieve a super-lyophobic surface, the liquid droplet on the roughened structures should be in the Cassie state. It is well known that micro/nano hierarchical surface textures are critically important for this effect.

3. Micro/nano hierarchical PDMS micro pillar array with surface texturing¹

We studied super-lyophobicity of a micro/nano-sized hierarchical PDMS pillar array against an oxidized gallium-based liquid metal alloy (Galinstan[®]) [35]. We first tested two types of

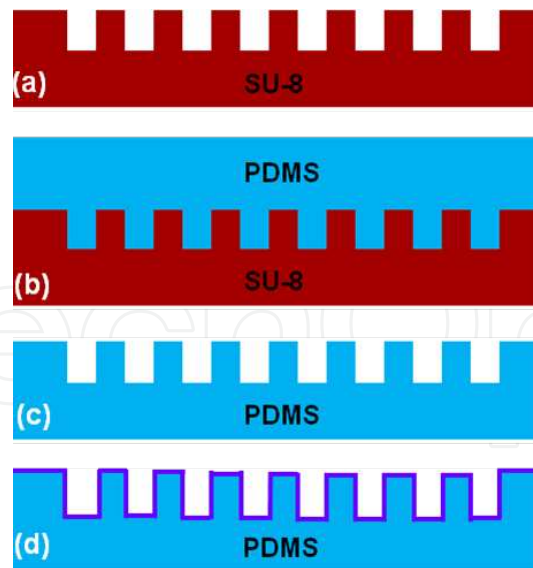


Figure 2. Fabrication sequence of the super-lyophobic micro-textured PDMS surfaces: (a) patterned SU-8 mold, (b) PDMS casting, (c) replicated PDMS, and (d) FC polymer deposition on the replicated PDMS micro arrays.

surface textured PDMS micro arrays: micro pillar arrays and micro ridge arrays. The vertical height of all PDMS micro textures was designed to be $45\ \mu\text{m}$. The fabrication of PDMS micro pillar and micro ridge arrays started with spin coating of SU-8 2025 photoresist (PR) (Micro-Chem Corp.) on a thermally grown oxidized Si wafer to get approximately $45\ \mu\text{m}$ -thick PR. The PR was soft-baked on a hot plate at 65°C for 2 minutes, 95°C for 3 minutes, and finally 65°C for 2 minutes. Then, a UV exposure dose of $140\ \text{mJ}/\text{cm}^2$ was applied by standard photolithography to create an inverse pattern of the target structure, and finally a post bake was applied with the same temperature and time of the soft bake. Finally, it was developed in SU-8 developer (propylene glycol methyl ether acetate) for 3 minutes under gentle stirring condition, and was cleaned with isopropyl alcohol and deionized (DI) water (Fig. 2a). After developing, the PDMS was casted over the PR mold; then it was cured at room temperature for a day to have flexible characteristics (Fig. 2b). After curing, PDMS was peeled off from the mold and it replicated arrays (Fig. 2c). An $80\ \text{nm}$ -thick fluorocarbon (FC) polymer was deposited on top of the PDMS arrays to enhance lyophobicity (Fig. 2d).

PDMS micro pillar arrays had various dimensions including $25\ \mu\text{m}$ pillar diameter and $25\ \mu\text{m}$ gap, $75\ \mu\text{m}$ diameter and $25\ \mu\text{m}$ gap, $75\ \mu\text{m}$ diameter and $100\ \mu\text{m}$ gap, $75\ \mu\text{m}$ diameter and $150\ \mu\text{m}$ gap, $75\ \mu\text{m}$ diameter and $200\ \mu\text{m}$ gap, and $75\ \mu\text{m}$ diameter and $250\ \mu\text{m}$ gap. PDMS micro ridge arrays had various widths and gaps ($25\ \mu\text{m}$ width and $25\ \mu\text{m}$ gap, $75\ \mu\text{m}$ width and $25\ \mu\text{m}$ gap, $75\ \mu\text{m}$ width and $100\ \mu\text{m}$ gap, $75\ \mu\text{m}$ width and $150\ \mu\text{m}$ gap, $75\ \mu\text{m}$ width and $200\ \mu\text{m}$ gap). Fig. 3 shows scanning electron microscope (SEM) images of the micro pillar arrays (Figs. 3a and 3b) and micro ridge arrays (Figs. 3c and 3d).

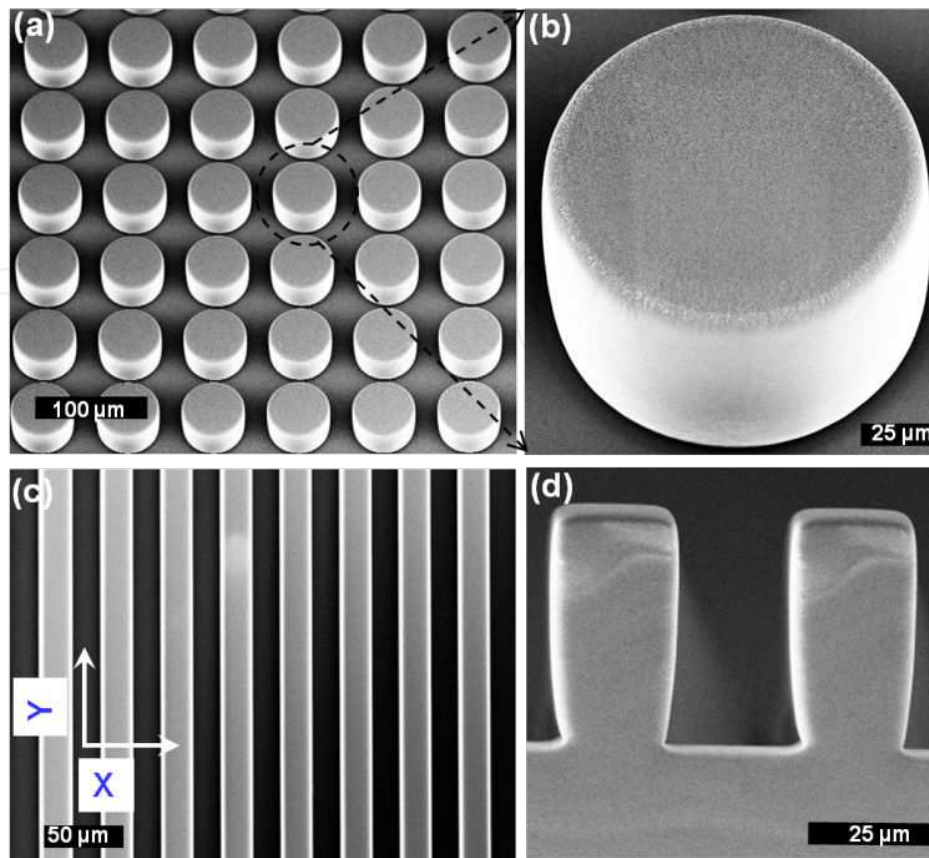


Figure 3. SEM images of PDMS micro arrays: (a) micro pillar array and (b) a close-up, 15° tilted view of a micro pillar; (c) micro ridge array and (d) a close-up side view of micro ridges.

Lyophobicity of textured surfaces was studied by measuring static and dynamic contact angles. Fig. 4 shows the images of static droplets of 7.8 μL oxidized Galinstan[®] on micro pillar arrays with the same pillar diameter (75 μm) but with various gap distances. Galinstan[®] droplet is not spherical due to the viscoelastic oxidized layer on the surface. The droplet on a 225 μm pitch distance (75 μm diameter and 150 μm gap) micro pillar array clearly formed a non-wetting Cassie state, confirmed by the presence of air pockets underneath the droplet (Fig. 4a). We observed the droplets on all micro pillar arrays with gap distances smaller than 150 μm formed a Cassie state, as it becomes more difficult for a Galinstan[®] to penetrate between micro pillars when the gap distance becomes smaller. On the other hand, the image of the Galinstan[®] droplet on a micro pillar array with 250 μm gap distance showed that the droplet penetrated between pillars, forming a fully wetted Wenzel state (Fig. 4c). We also found that the droplets on any micro pillar array with gap distance larger than 250 μm showed Wenzel state. There were intermediate transition states between the Cassie and the Wenzel states. Figure 4b shows Galinstan[®] droplet on a 200 μm gap distance. The droplet penetrated into a portion of the texture, but we could observe some intact air pockets as well. It was also found that micro ridge arrays with gap distances smaller than 150 μm (75 μm ridge width) showed Cassie state. Table 1 shows static contact angles for various pitch distances in the range of 50 to 225 μm .

Since the contact area of the micro pillar arrays is smaller than that of the micro ridge arrays for the same pitch distances, the static contact angle of the micro pillar arrays is relatively larger than that of the micro ridge arrays. The static contact angle of 139.1° on a pillar array with $75\ \mu\text{m}$ diameter and $150\ \mu\text{m}$ gap distance (solid fraction = 0.087) is not remarkably high, considering the extremely low solid fraction, due to the highly hysteretic behavior of the oxidized Galinstan[®].

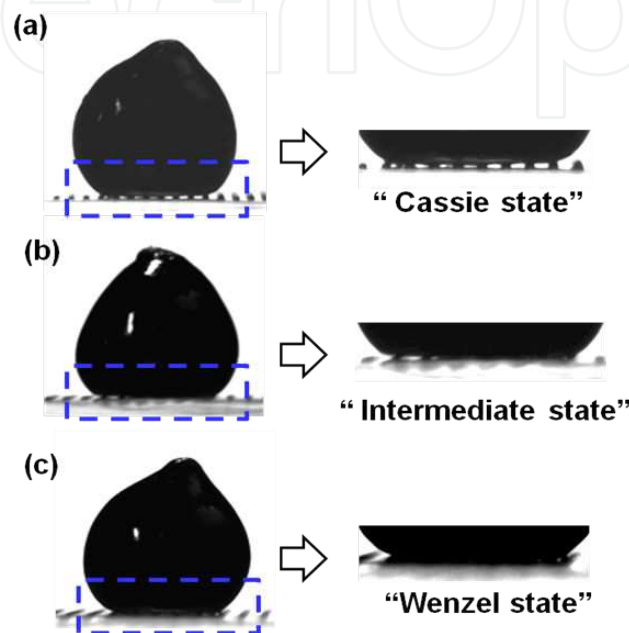


Figure 4. A $7.8\ \mu\text{L}$ oxidized Galinstan[®] droplet on (a) $150\ \mu\text{m}$ gap micro pillar array showing a non-wetting Cassie state, (b) $200\ \mu\text{m}$ gap micro pillar array showing an intermediate transition state, and (c) $250\ \mu\text{m}$ gap micro pillar array (no air pockets) showing a fully wetted Wenzel state. The diameter of all micro pillars is $75\ \mu\text{m}$.

Substrates	Diameter / width (μm)	Pitch distance (μm)	Solid fraction (f_s)	Static contact angle ($^\circ$)
Micro pillar array	25	50	0.196	141.6 ± 0.2
		100	0.442	135.8 ± 1.2
	75	175	0.144	140.6 ± 3.5
		225	0.087	139.1 ± 4.4
Micro ridge array	25	50	0.500	139.5 ± 1.1
		100	0.750	131.4 ± 1.8
	75	175	0.429	133.5 ± 3.7
		225	0.334	137.9 ± 1.2

Table 1. Static contact angles for a $7.8\ \mu\text{L}$ oxidized Galinstan[®] droplet on PDMS micro pillar and micro ridge arrays.

The dynamic contact angles were measured in the same way as described in the previous section. Table 2 shows dynamic contact angles of the oxidized Galinstan[®] droplet on micro pillar arrays and micro ridge arrays with various dimensions. For the micro ridge arrays, contact angles were measured from two different viewing directions when the droplet was advancing/receding: across the ridges (X direction; see Fig. 3c) and along the ridges (Y direction).

Substrates	Pitch distance (μm)	Solid fraction (f_s)	Dynamic contact angles ($^\circ$)		Contact angle hysteresis ($^\circ$)
			Adv.	Rec.	
Micro pillar array	50	0.196	179.0	75.3	103.7
	100	0.442	163.5	51.3	112.2
	175	0.144	160.5	77.9	82.6
	225	0.087	153.5	51.0	102.5
Micro ridge array (X direction, across the ridges)	50	0.500	161.0	50.0	111.0
	100	0.750	161.8	20.5	141.3
	175	0.429	161.5	43.3	118.2
	225	0.334	163.5	40.0	123.5
Micro ridge array (Y direction, along the ridges)	50	0.500	155.3	38.3	117.0
	100	0.750	156.8	16.8	140.0
	175	0.429	156.8	32.5	124.3
	225	0.334	158.3	37.0	121.3

Table 2. Dynamic contact angles of the oxidized Galinstan[®] droplet.

For simple fluids, such as water or hexadecane, the contact angle hysteresis when a droplet advances/recedes along the ridges (Y direction) is less than that on micro pillar arrays with the same solid fraction as, for micro pillar array, the solid fraction near the contact line significantly changes between advancing and receding droplets [36]. However, for Galinstan[®], we found that the contact angle hystereses on the micro ridge arrays in both directions (X and Y) are larger than those on the micro pillar arrays. We suspect that the viscoelasticity of Galinstan[®], combined with its extreme wettability, causes the receding of the droplet from the top of pillars and ridges virtually impossible, leading to the discrepancy between the conventional model of hysteresis and the observed values. The pillar array with 75 μm diameter and 100 μm gap distance showed the smallest contact angle hysteresis (82.6 $^\circ$) among all textured surfaces. Nonetheless, the residue of the oxidized Galinstan[®] was still left on the surface after receding even though the droplet formed the Cassie state (Fig. 5).

Although there was decrease in contact angle hysteresis from those of the various flat surfaces to the surfaces textured with PDMS micro arrays, it turned out that the naturally oxidized Galinstan[®] droplet did not completely dewet from all tested surfaces, regardless of the shape and pitch distance of the PDMS micro arrays.

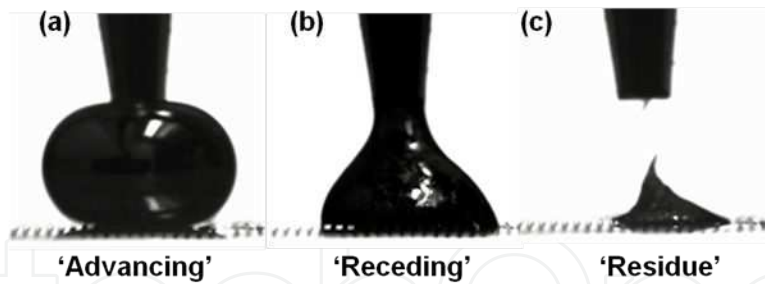


Figure 5. Advancing angle (160.5°), receding angle (77.9°), and residual state of the oxidized Galinstar[®] on the micro pillar array with $75\ \mu\text{m}$ diameter and $100\ \mu\text{m}$ gap distance.

To further improve lyophobicity of the PDMS micro arrays, we further studied lyophobicity of multi-scale surface textured PDMS micro pillar arrays. The fabrication of multi-scale surface textured PDMS micro pillar arrays started with triple-spin coating of AZP4620 PR (AZ Electronic materials) on a thermally oxidized Si wafer to get approximately a $45\ \mu\text{m}$ -thick PR. The PR was intentionally under-baked in a convection oven at 88°C (typical soft-bake temperature is 110°C on a hot plate). Then, the PR was under-exposed with the exposure dose of $800\ \text{mJ}/\text{cm}^2$ (typical exposure dose is $>1,600\ \text{mJ}/\text{cm}^2$) [37]. After developing the PR with diluted AZ400K (AZ Electronic materials) (Fig. 6a), the PDMS was casted over the PR mold and it was cured at room temperature for one day (Fig. 6b). The replicated PDMS showed multi-scale surface textured micro pillar array (Fig. 6c). The $80\ \text{nm}$ -thick FC polymer was then deposited on the replicated multi-scale surface textured PDMS micro pillar array to enhance the lyophobicity (Fig. 6d). Fig. 7 shows the SEM image of multi-scale surface textured PDMS micro pillar arrays.

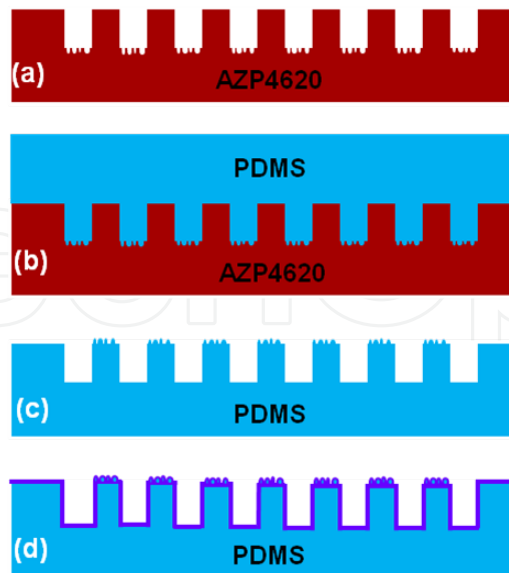


Figure 6. Fabrication sequence of the multi-scale surface textured PDMS micro pillars: (a) fabrication of AZP4620 mold with multi-scale textures (under-baked and under-exposed), (b) PDMS casting, (c) replicated PDMS, (d) FC polymer deposition on the replicated multi-scale surface textured PDMS micro pillars.

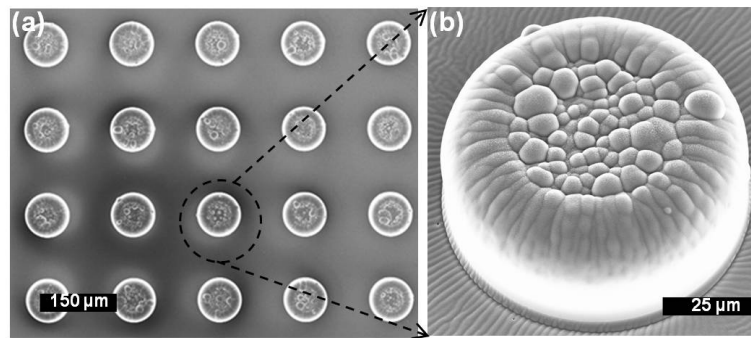


Figure 7. SEM images of (a) multi-scale surface textured PDMS micro pillar arrays and (b) close-up view of a single pillar that is textured with additional roughness.

The static and dynamic contact angles were studied on the multi-scale PDMS micro pillar arrays for the naturally oxidized Galinstan[®] droplet. Fig. 8 shows static contact angles as a function of pitch distance in the range of 50 ~ 225 μm for the multi-scale PDMS micro pillar arrays as well as PDMS micro pillar and ridge arrays.

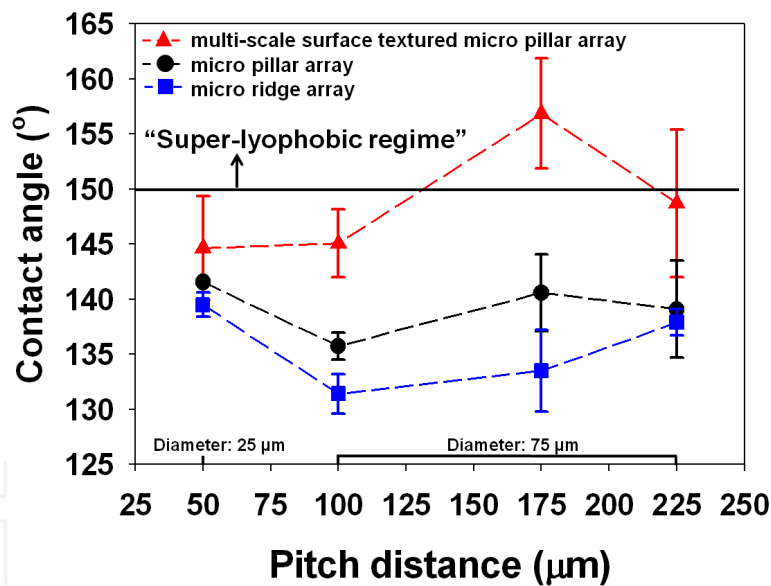


Figure 8. Contact angles of a 7.8 μL oxidized Galinstan[®] droplet on a multi-scale surface textured micro pillar array, micro pillar, and ridge arrays.

The static contact angle of the Galinstan[®] droplet on the FC polymer-deposited flat PDMS surface was 125.4°. The contact angle on the 100 μm pitch PDMS micro ridge array, on the other hand, turned out to be 131.4°, showing only a small improvement in lyophobicity of the surface. However, the contact angle of the Galinstan[®] droplet on the multi-scale surface patterned PDMS micro pillar array was found to be substantially higher, to be close to the super-lyophobic regime ($> 150^\circ$). The 175 and 225 μm pitch distance multi-scale surface textured PDMS micro pillar arrays showed contact angles of 156.9° and 148.7°, respectively.

Regardless of the pitch distance, the static contact angle on the multi-scale surface patterned micro pillar arrays is the highest compared to other textured surfaces. We believe that this is attributed to the lower solid fraction (f_s) based on the additional roughness of the multi-scale surface pattern on the micro pillar arrays. The solid fraction of the multi-scale surface textured micro pillar array cannot be directly calculated because the surface is irregularly patterned. Therefore, the solid fraction of the multi-scale surface textured PDMS micro pillar array was estimated by comparing static contact angles of the micro pillar arrays to those of the multi-scale surface textured PDMS micro pillar arrays. The experimentally determined solid fraction of the 175 μm pitch distance multi-scale surface patterned micro pillar array is 0.105 which is much smaller than that of the micro ridge array (0.429) and of the micro pillar array (0.144).

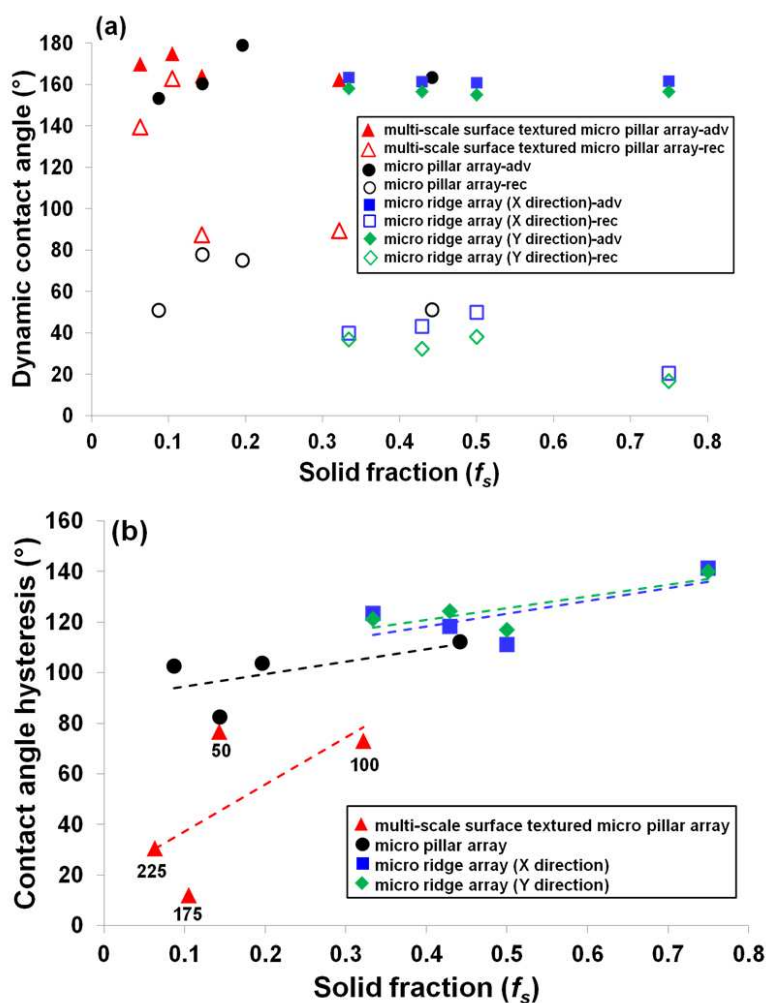


Figure 9. (a) The measured advancing and receding contact angles, and (b) contact angle hysteresis of multi-scale surface patterned micro pillar arrays, micro pillar and ridge arrays as a function of solid fraction (numbers in the graph indicates pitch distance in μm). The colored dot lines are trend lines for multi-scale surface patterned micro pillar arrays, micro pillar and ridge arrays.

Fig. 9a shows the advancing and receding contact angles as a function of the solid fraction of micro pillar arrays, micro ridge arrays and multi-scale surface patterned micro pillar arrays.

The advancing contact angles are larger than 150° for all micro arrays, but the receding contact angles vary drastically as a function of the solid fraction. Of various micro arrays, the $175\ \mu\text{m}$ pitch distance ($75\ \mu\text{m}$ diameter pillar and $100\ \mu\text{m}$ gap) multi-scale surface patterned PDMS micro pillar arrays showed the largest advancing and receding contact angles of approximately 175° and 163° (Figs. 10a and 10b), respectively. Fig. 9b shows the contact angle hysteresis as a function of the solid fraction for various micro arrays. The contact angle hysteresis increases as the solid fraction increases. The smallest contact angle hysteresis (12°) was obtained on the $175\ \mu\text{m}$ pitch distance multi-scale surface patterned PDMS micro pillar array, while the $100\ \mu\text{m}$ pitch distance micro ridge array (X-direction) showed the largest contact angle hysteresis of 140° .

With the smallest contact angle hysteresis, we found that there remains no residue of oxidized Galinstan[®] after the droplet recedes from the surface (Fig. 10c) with the $175\ \mu\text{m}$ pitch distance multi-scale surface patterned PDMS micro pillar array.

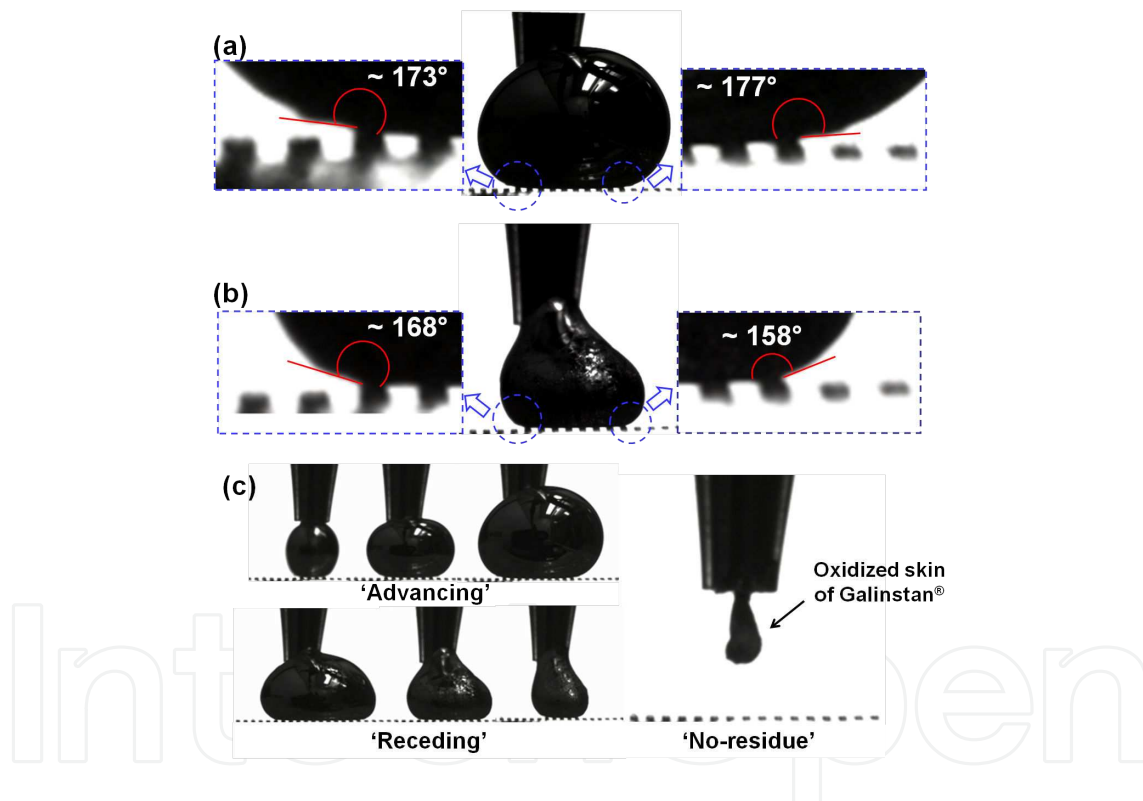


Figure 10. Optical images of an oxidized Galinstan[®] droplet on the multi-scale surface patterned PDMS micro pillar arrays (pitch distance $175\ \mu\text{m}$) during dynamic contact angle test: (a) advancing contact angle ($\theta_{adv} = 175^\circ$), (b) receding contact angle ($\theta_{rec} = 163^\circ$), and (c) evidence of no-residue after receding from the surface.

4. Micro/nano hierarchical carbon nanotube on PDMS²

CNTs show a unique material property of super-repellency against both water and oil. This is attributed to its hierarchical micro/nano structures, as well as its chemical inertness. While an

individual CNT is nanometer scale, bundles of CNT forests have a micrometer scale creating a micro/nano hierarchical surface. Using this property, the super-lyophobicity of CNT on PDMS against the oxidized gallium-based liquid metal is reviewed in this section [38].

Fig. 11 shows the schematics of transferring CNT onto PDMS sheets. First, vertically aligned multi-wall carbon nanotube (MWCNT) was grown by chemical vapor deposition (CVD) process on an iron catalyst deposited by e-beam evaporation (Fig. 11a). Approximately 400 μm tall vertically aligned MWCNT was grown on a piece of Si wafer (9 mm \times 13.5 mm) for 5 minutes at 780°C with C_2H_2 , He, and H_2 gas [39]. RTV 615 A and B (HISCO, Inc.) were mixed in 10:1 volume ratio and the calculated volume (4.5 mL) of PDMS was poured to make approximately 500 μm -thick PDMS on a Teflon substrate (9.5 cm \times 9.5 cm) placed on a petri dish. The poured PDMS was cured at room temperature for 24 hours in air environment. It is known that the higher mechanical flexibility of PDMS can be obtained with lower curing temperature [40]. In order to transfer the MWCNT onto the PDMS sheet, we utilized a nano-imprinter (Obducat Nano-Imprinter NIL-2.5" Imprint). Even though the transferring of MWCNT onto the PDMS can be simply achieved by stamping [41, 42], we applied force to have more uniform contact so that the CNT can be well transferred. We flipped the CNT-grown Si wafer upside down and placed it on top of 500 μm -thick flexible PDMS. Then, in order to imprint, we applied a force of 400 N for 20 seconds. (Fig. 11c). After the Si wafer was removed, we found that the CNT on Si was well transferred onto the PDMS sheet (Fig. 11d).

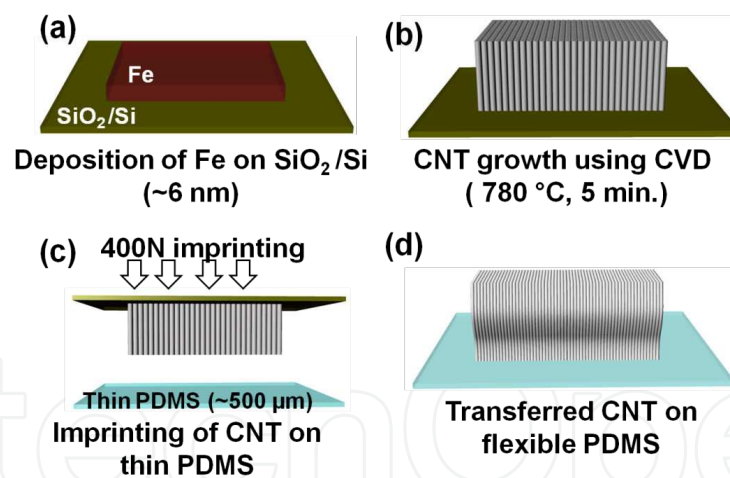


Figure 11. Fabrication sequence of the stretchable and bendable super-lyophobic CNT on PDMS sheet: (a) iron catalyst on Si, (b) vertically aligned CNT growth on Si, (c) imprinting CNT onto PDMS sheet, and (d) transferred CNT on PDMS sheet.

Fig. 12 shows optical and SEM images of the grown CNT on Si (Fig. 12a) and the transferred CNT on PDMS sheet (Fig. 12b). The grown CNT on Si was vertically aligned and its average height was 400 μm (Fig. 12c). The top-view SEM image of the grown CNT on Si clearly shows

micron-scale bundled MWCNT, while individual CNTs show nanoscale surface morphology (Fig. 12d). After transferring, the height of the transferred MWCNT on the PDMS sheet, which was still vertically aligned, shrunk from 400 μm to 60 μm (Fig. 12e). We found that even after the transfer process, it maintained micro/nano hierarchical surface morphology (Fig. 12f) but the size of micron scale morphology was reduced.

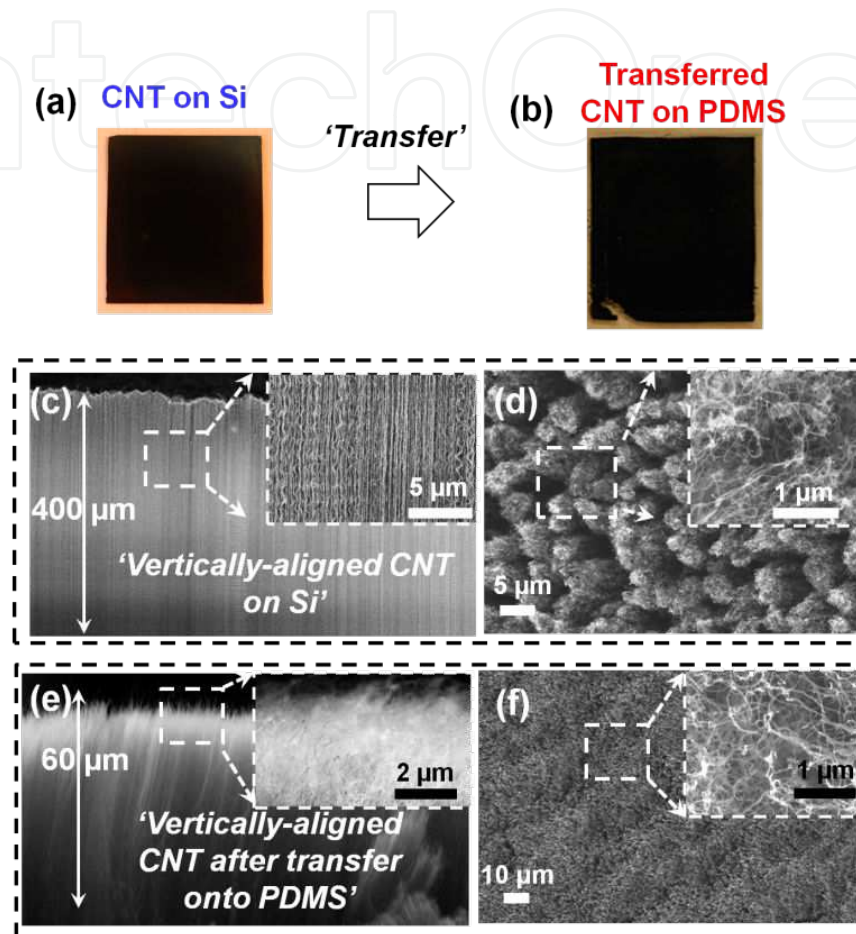


Figure 12. Optical and SEM images of CNT on Si and PDMS: optical images of (a) grown CNT on Si; (b) transferred CNT on PDMS sheet; (c) side-view SEM image of the vertically aligned CNT on Si; (d) top-view SEM image of the CNT showing micro/nano scale mixed morphology; (e) side-view SEM image of vertically aligned CNT after transfer onto the PDMS sheet; and (f) top-view SEM image of micro/nano surface morphology after the transfer.

In order to study the lyophobicity of the transferred CNT on PDMS sheet under mechanical deformation against the oxidized gallium-based liquid metal alloy (Galinstan[®]), we stretched and bent the CNT on the PDMS sheet. PDMS is well known for its physical flexibility due to its extremely low Young's modulus (< 4 MPa) [43]. The CNT on PDMS sheet was stretched by 50% and 100% ratio and bent with a curvature of 0.1 mm^{-1} and 0.4 mm^{-1} , respectively, as shown in Fig. 13.

Fig. 14 shows the contact angle measurement of a liquid droplet on a lyophobic flat surface and a negatively curved surface. The intrinsic contact angle (θ_{il} , θ_{ir}) on the flat surface is formed by a straight line tangential to the droplet at its left side (L_{il}) or right side (L_{ir}) with a horizontal

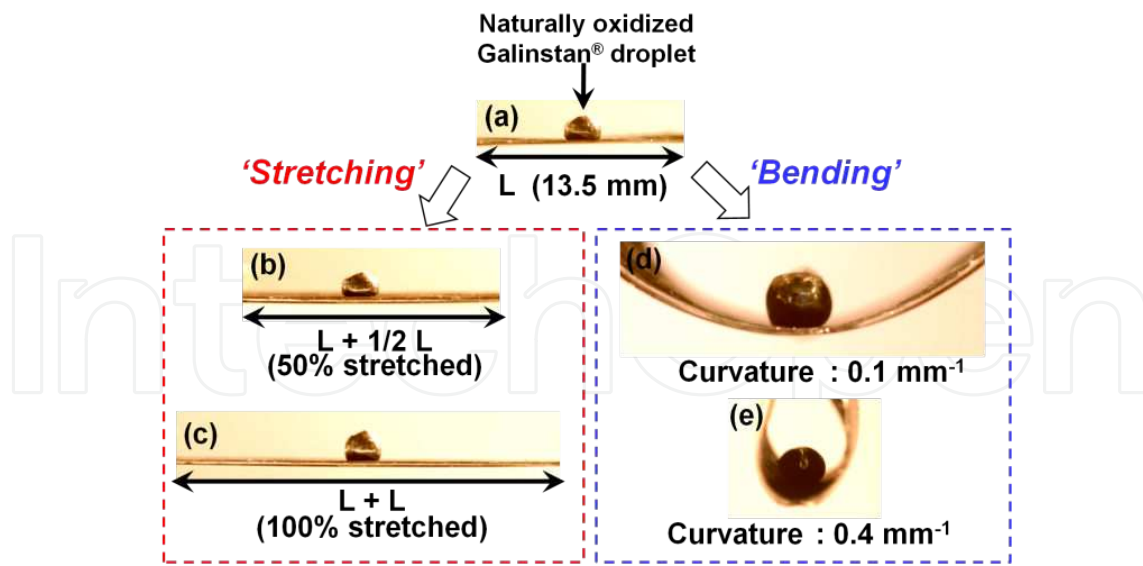


Figure 13. Stretchable and bendable CNT on PDMS sheet: (a) Galinstan[®] droplet on CNT on PDMS sheet, (b, c) 50% and 100% stretched CNT on PDMS sheet, and (d, e) bent CNT on PDMS sheet with a curvature of 0.1 mm^{-1} and 0.4 mm^{-1} .

line (L_h). There is, however, no horizontal line for the contact angle measurement on a curved surface. Thus, we assume the shape of the curved substrate to be a part of a circle whose center is defined as 'o'. We then identify the intersection point between the circle and the outline of the droplet. Tangential lines drawn at the left and right intersection points are used as the bottom lines to define the contact angles. The left contact angle (θ_{cl}) of a droplet on the curved surface is the exterior angle formed by a tangential line (l_{cl}) to the droplet at the left side and the tangential line to the circle at the left intersection point (l_{tl}). In the same manner, the right contact angle (θ_{cr}) of a liquid droplet on the curved surface is determined.

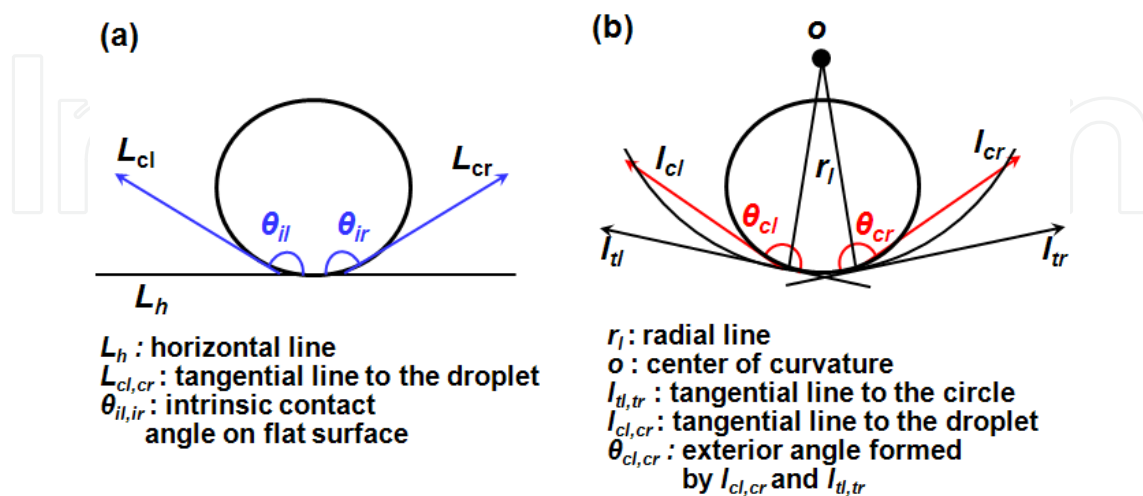


Figure 14. Schematics of contact angle measurement of a liquid droplet on (a) a lyophobic flat surface and (b) a curved surface.

We measured static and dynamic contact angles to study the lyophobicity of various surfaces against the oxidized gallium-based liquid metal alloy (Galinstan[®]): i) CNT grown on Si substrate; ii) transferred CNT on PDMS sheet; iii) stretched CNT on PDMS with 50% and 100% extension ratio; and iv) bent CNT on PDMS with a curvature of 0.1 mm⁻¹ and 0.4 mm⁻¹.

Fig. 15 shows static contact angles of ~7.8 μL oxidized Galinstan[®] droplet on various surfaces. We found that all static contact angles were very close to or greater than 150°, which is a super-lyophobic regime. This is attributed to micro/nano scale combined hierarchical structure of the vertically aligned CNT. As shown in Figs. 12e and 12f, the transferred CNT on PDMS sheet maintained a vertically aligned structure as well as micro/nano scale combined surface morphology. As a result, on the transferred CNT on PDMS a very similar static contact angle of 156.2 ± 5.8° compared to that of the CNT on Si substrate was obtained.

Comparing to that of the CNT on PDMS without stretching, the contact angles on the stretched CNT on PDMS sheet with a 50% and 100% extension ratio were slightly decreased. We believe that the vertically aligned CNT may be slightly tilted or collapsed down so that the surface morphology was changed by stretching the PDMS substrate. However, the static contact angle change before and after the stretching is in the range of error bar and there is no clear trend of change in the static contact angle due to stretching. It is noted that they are still in the super-lyophobic regime even with the decreased static contact angles. The contact angle of the oxidized gallium-based liquid metal (Galinstan[®]) droplet placed on the negatively curved surface with a curvature of 0.1 mm⁻¹ was slightly decreased to 153.8 ± 5°. The contact angle on the curved surface with a curvature of 0.4 mm⁻¹, however, is essentially the same (156.8 ± 3.3°) compared to that of the flat CNT on PDMS which is 156.2 ± 5.8°. Again, as those contact angles are in the range of error bar, we can conclude that there is no significant change in hierarchical micro/nano dual scale surface morphology of the CNT on PDMS by bending or stretching.

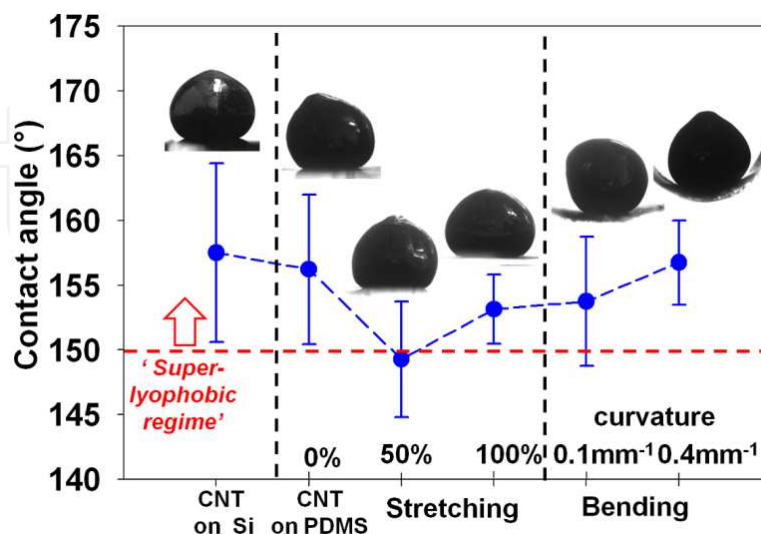


Figure 15. Static contact angle of ~7.8 μL oxidized Galinstan[®] droplet on various surfaces.

In conjunction with static contact angle, dynamic contact angle is another important indicator of lyophobicity, especially for the droplet manipulation. We measured dynamic contact angles of the gallium-based liquid metal alloy (Galinstan[®]) on the CNT on Si substrate, as well as CNT on PDMS with and without bending and stretching (Fig. 16). The red-colored circles indicate advancing contact angles and blue-colored squares indicate receding contact angles, respectively. The advancing and receding contact angles of the oxidized Galinstan[®] droplet on the CNT on Si substrate were 165° and 161° (optical images of the advancing and receding angle measurement are shown in the left-side inset), respectively. As a result, the contact angle hysteresis (advancing contact angle - receding contact angle) was found to be 4°. The lyophobicity seemed somewhat decreased after the CNT transfer process. The advancing contact angles on the transferred CNT on PDMS sheet, the stretched and bent CNT on PDMS sheet were all greater than 150°. The receding contact angles of the CNT on PDMS before and after bending and stretching were in the range of 133° ~ 140°. The smallest contact angle hysteresis of ~11° (optical images of the advancing and receding angle measurement are shown in the right-side inset) was found on the 100% stretched CNT on PDMS sheet and the largest contact angle hysteresis of ~22° was found on the 50% stretched CNT on PDMS sheet. The contact angle hysteresis of the transferred CNT on PDMS was ~19°.

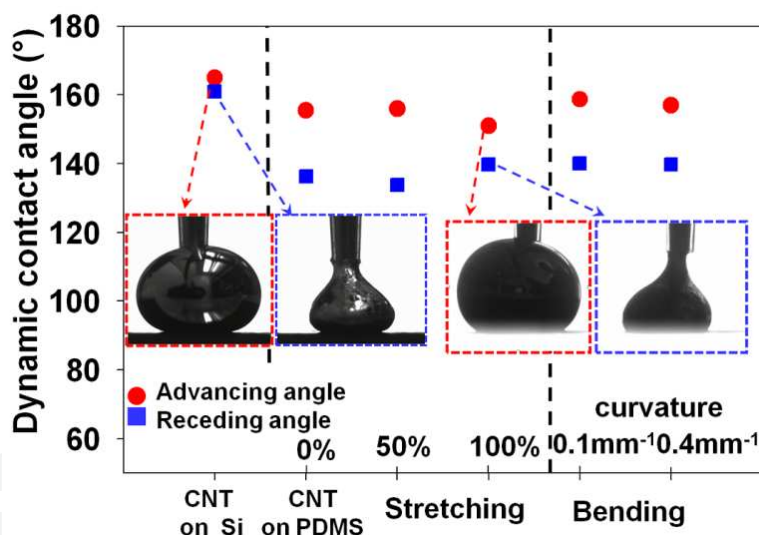


Figure 16. Dynamic contact angle of oxidized Galinstan[®] on various surfaces.

Based on the static and dynamic contact angle measurements of the oxidized Galinstan[®] droplet, we expected that the transferred CNT on PDMS sheet can be used as a stretchable and bendable super-lyophobic surface against the oxidized gallium-based liquid metal droplet. To confirm this, we carried out a series of bouncing tests for the transferred CNT on PDMS sheet with and without stretching.

The oxidized gallium-based liquid metal droplet (~7.8 μL) was dropped 3.5 cm above the surface and impacted the substrate while the movement of the droplet was recorded using a high-speed camera (Fastcam SA4, Photron Limited, Tokyo, Japan) with 1,000 frames per

second. Note that the oxidation of the droplet is nearly instant in ambient air environment that the Galinstan[®] droplet becomes oxidized on the fly and it is already fully oxidized by the moment of impact at the surface. Fig. 17 shows a series of time-lapse images of bouncing of the oxidized Galinstan[®] droplet from the surface of the CNT on Si substrate, the transferred CNT on PDMS sheet with and without stretching. Before the droplet hit the surface, the shape of the droplet is not spherical due to its viscoelastic oxide layer. Nonetheless, after the oxidized liquid metal droplet hit the surfaces, the droplet spread on the surfaces and readily bounced off from all surfaces. The results from the bouncing tests indicated that these surfaces have anti-wetting characteristics against the oxidized gallium-based liquid metal droplet. In conjunction with the measured static and dynamic contact angles, this confirms that the transferred CNT on PDMS sheet is a stretchable super-lyophobic surface against the oxidized gallium-based liquid metal droplet.

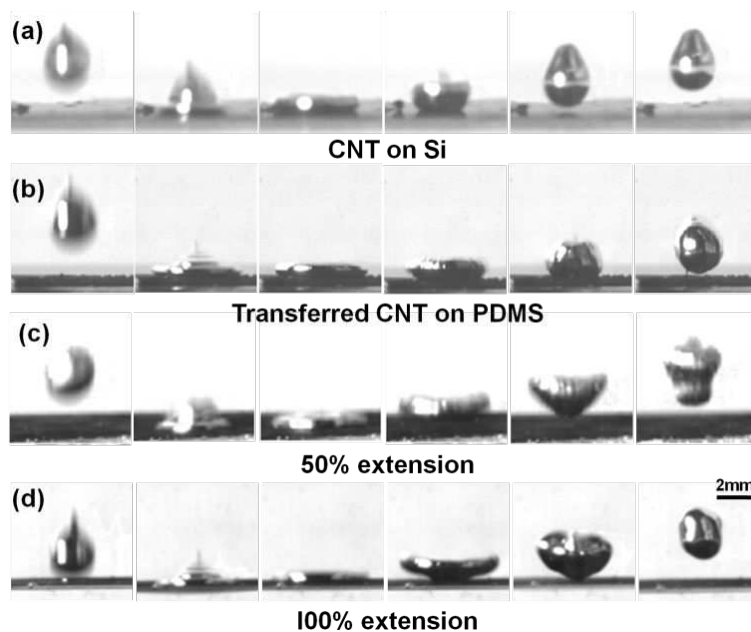


Figure 17. A series of time-lapse images of bouncing of the Galinstan[®] droplet from the surface of (a) CNT on Si, (b) transferred CNT on PDMS sheet without strain, (c) CNT on PDMS with 50% strain, and (d) with 100% strain.

To test anti-wetting characteristics of the bent CNT on PDMS sheet, we carried out rolling tests. The CNT on PDMS sheet were bent to have negatively curved surfaces with curvature of 0.1 mm^{-1} and 0.4 mm^{-1} as shown in Fig. 13. On the curved surface with a curvature of 0.1 mm^{-1} and 0.4 mm^{-1} , the oxidized liquid metal droplet with volume of $\sim 7.8 \text{ }\mu\text{L}$ and $\sim 1.6 \text{ }\mu\text{L}$ were utilized, respectively, for rolling tests.

Fig. 18 shows a series of time-lapse images of the rolling Galinstan[®] droplet on the negatively curved CNT on PDMS surfaces. The droplet was dropped from the left-end edge of the bent CNT on PDMS. On the curved surface with a curvature of 0.1 mm^{-1} and 0.4 mm^{-1} , the droplet was readily moved to the right side of the curved surface with an average speed of ~ 11.9 and $\sim 26.2 \text{ cm/sec}$, respectively, and it was stopped at the lowest point of the curved surface. After

the rolling test, the surface of the CNT on PDMS was thoroughly inspected and it was found that there was no oxidized liquid metal residue remaining after the rolling of the liquid metal droplet.

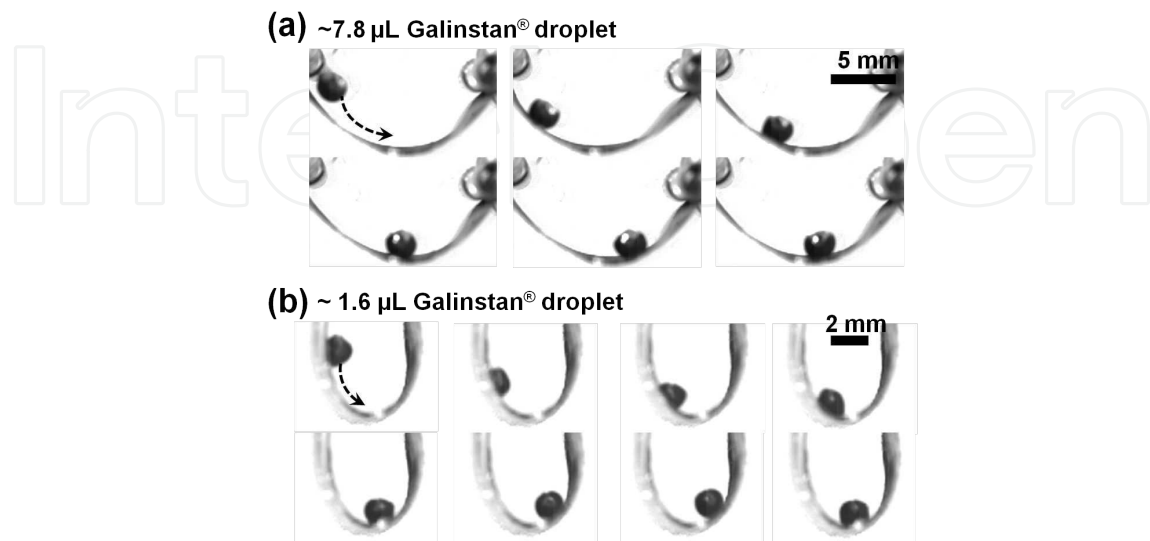


Figure 18. A series of time-lapse images of rolling of Galinstan[®] droplet on the bent CNT on PDMS sheet with a curvature of (a) 0.1 mm^{-1} and (b) 0.4 mm^{-1} .

5. Conclusions

We have reviewed concepts of ‘lyophobic/lyophilic’ and studied wetting phenomena on the planar and roughened surfaces: Young’s relation and Cassie/Wenzel model. These theoretical studies emphasize that micro/nano hierarchical structure can be attributed to the super-lyophobicity against the oxidized gallium-based liquid metal alloy. As demonstrations of micro/nano hierarchical structure-based surfaces, the PDMS micro pillar array with dual scale surface texturing and CNT on PDMS are described.

Author details

Daeyoung Kim^{1*} and Jeong-Bong Lee²

*Address all correspondence to: jokuksarang64@gmail.com

1 Department of Electrical Engineering, Korea Army Academy, Yeong-cheon, Kyung-sang-buk-do, South Korea

2 Department of Electrical Engineering, The University of Texas at Dallas, Richardson, TX, USA

References

- [1] T. Liu, P. Sen, and C.-J. Kim, "Characterization of Nontoxic Liquid-Metal Alloy Gallinstan for Applications in Microdevices," *Journal of Microelectromechanical Systems*, vol. 21, p. 443, 2012.
- [2] K.-Q. Ma and J. Liu, "Heat-driven liquid metal cooling device for the thermal management of a computer chip," *Journal of Physics D: Applied Physics*, vol. 40, p. 4722, 2007.
- [3] H.-J. Kim, C. Son, and B. Ziaie, "A multiaxial stretchable interconnect using liquid-alloy-filled elastomeric microchannels," *Applied Physics Letters*, vol. 92, p. 011904, 2008.
- [4] C. Ladd, J.-H. So, J. Muth, and M. D. Dickey, "3D Printing of Free Standing Liquid Metal Microstructures," *Advanced Materials*, vol. 25, p. 5081, 2013.
- [5] B. Aissa, M. Nedil, M. A. Habib, E. Haddad, W. Jamroz, D. Therriault, *et al.*, "Fluidic patch antenna based on liquid metal alloy/single-wall carbon-nanotubes operating at the S-band frequency," *Applied Physics Letters*, vol. 103, p. 063101, 2013.
- [6] S. Cheng, A. Rydberg, K. Hjort, and Z. Wu, "Liquid metal stretchable unbalanced loop antenna," *Applied Physics Letters*, vol. 94, p. 144103, 2009.
- [7] G. J. Hayes, J.-H. So, A. Qusba, M. D. Dickey, and G. Lazzi, "Flexible Liquid Metal Alloy (EGaIn) Microstrip Patch Antenna," *Antennas and Propagation, IEEE Transactions on*, vol. 60, p. 2151, 2012.
- [8] A. J. King, J. F. Patrick, N. R. Sottos, S. R. White, G. H. Huff, and J. T. Bernhard, "Microfluidically Switched Frequency-Reconfigurable Slot Antennas," *Antennas and Wireless Propagation Letters, IEEE*, vol. 12, p. 828, 2013.
- [9] M. Kubo, X. Li, C. Kim, M. Hashimoto, B. J. Wiley, D. Ham, *et al.*, "Stretchable Microfluidic Radiofrequency Antennas," *Advanced Materials*, vol. 22, p. 2749, 2010.
- [10] C. Shi, W. Zhigang, P. Hallbjorner, K. Hjort, and A. Rydberg, "Foldable and Stretchable Liquid Metal Planar Inverted Cone Antenna," *Antennas and Propagation, IEEE Transactions on*, vol. 57, p. 3765, 2009.
- [11] D. Kim, R. G. Pierce, R. Henderson, S. J. Doo, K. Yoo, and J.-B. Lee, "Liquid metal actuation-based reversible frequency tunable monopole antenna," *Applied Physics Letters*, vol. 105, p. 234104, 2014.
- [12] T. S. Kasirga, Y. N. Ertas, and M. Bayindir, "Microfluidics for reconfigurable electromagnetic metamaterials," *Applied Physics Letters*, vol. 95, p. 214102, 2009.
- [13] J. Wang, S. Liu, S. Guruswamy, and A. Nahata, "Reconfigurable liquid metal based terahertz metamaterials via selective erasure and refilling to the unit cell level," *Applied Physics Letters*, vol. 103, p. 221116, 2013.

- [14] N. Hallfors, A. Khan, M. D. Dickey, and A. M. Taylor, "Integration of pre-aligned liquid metal electrodes for neural stimulation within a user-friendly microfluidic platform," *Lab on a Chip*, vol. 13, p. 522, 2013.
- [15] H. Huan and L. Chang, "Characterizations and optimization of electrical contact between nanocomposite elastomer and metal," in *Solid-State Sensors, Actuators and Microsystems Conference, 2009. TRANSDUCERS 2009. International, 2009*, p. 1103.
- [16] B. L. Mellor, N. A. Kellis, and B. A. Mazzeo, "Note: Electrode polarization of Galinstan electrodes for liquid impedance spectroscopy," *Review of Scientific Instruments*, vol. 82, p. 046110, 2011.
- [17] J.-H. So and M. D. Dickey, "Inherently aligned microfluidic electrodes composed of liquid metal," *Lab on a Chip*, vol. 11, p. 905, 2011.
- [18] J.-H. So, H.-J. Koo, M. D. Dickey, and O. D. Velev, "Ionic Current Rectification in Soft-Matter Diodes with Liquid-Metal Electrodes," *Advanced Functional Materials*, vol. 22, p. 625, 2012.
- [19] F. Scharmann, G. Cherkashinin, V. Breternitz, C. Knedlik, G. Hartung, T. Weber, *et al.*, "Viscosity effect on GaInSn studied by XPS," *Surface and Interface Analysis*, vol. 36, p. 981, 2004.
- [20] D. Zrnica and D. S. Swatik, "On the resistivity and surface tension of the eutectic alloy of gallium and indium," *Journal of the Less Common Metals*, vol. 18, p. 67, 1969.
- [21] D. Kim, P. Thissen, G. Viner, D.-W. Lee, W. Choi, Y. J. Chabal, *et al.*, "Recovery of Nonwetting Characteristics by Surface Modification of Gallium-Based Liquid Metal Droplets Using Hydrochloric Acid Vapor," *ACS Applied Materials & Interfaces*, vol. 5, p. 179, 2013.
- [22] G. Li, M. Parmar, D. Kim, J.-B. Lee, and D.-W. Lee, "PDMS based coplanar microfluidic channels for the surface reduction of oxidized Galinstan," *Lab on a Chip*, vol. 14, p. 200, 2014.
- [23] V. Sivan, S.-Y. Tang, A. P. O'Mullane, P. Petersen, N. Eshtiaghi, K. Kalantar-zadeh, *et al.*, "Liquid Metal Marbles," *Advanced Functional Materials*, vol. 23, p. 144, 2013.
- [24] D. Kim and J.-B. Lee, "Magnetic-field-induced liquid metal droplet manipulation," *Journal of the Korean Physical Society*, vol. 66, p. 282, 2015.
- [25] M. R. Khan, C. Trlica, and M. D. Dickey, "Recapillarity: Electrochemically Controlled Capillary Withdrawal of a Liquid Metal Alloy from Microchannels," *Advanced Functional Materials*, vol. 25, p. 671, 2015.
- [26] R. Blossey, "Self-cleaning surfaces [mdash] virtual realities," *Nature Materials*, vol. 2, p. 301, 2003.
- [27] R. Fürstner, W. Barthlott, C. Neinhuis, and P. Walzel, "Wetting and Self-Cleaning Properties of Artificial Superhydrophobic Surfaces," *Langmuir*, vol. 21, p. 956, 2005.

- [28] A. Nakajima, K. Hashimoto, T. Watanabe, K. Takai, G. Yamauchi, and A. Fujishima, "Transparent Superhydrophobic Thin Films with Self-Cleaning Properties," *Langmuir*, vol. 16, p. 7044, 2000.
- [29] S. Farhadi, M. Farzaneh, and S. A. Kulinich, "Anti-icing performance of superhydrophobic surfaces," *Applied Surface Science*, vol. 257, p. 6264, 2011.
- [30] L. Cao, A. K. Jones, V. K. Sikka, J. Wu, and D. Gao, "Anti-Icing Superhydrophobic Coatings," *Langmuir*, vol. 25, p. 12444, 2009.
- [31] B. Bhushan, Y. C. Jung, and K. Koch, "Micro-, nano- and hierarchical structures for superhydrophobicity, self-cleaning and low adhesion," *Philosophical Transactions of the Royal Society A: Mathematical, Physical and Engineering Sciences*, vol. 367, p. 1631, 2009.
- [32] T. Young, "An Essay on the Cohesion of Fluids," *Philosophical Transactions of the Royal Society of London*, vol. 95, p. 65, 1805.
- [33] R. N. Wenzel, "Resistance of Solid Surfaces to Wetting by Water," *Industrial & Engineering Chemistry*, vol. 28, p. 988, 1936.
- [34] S. Baxter and A. B. D. Cassie, "8—The Water Repellency of Fabrics and a New Water Repellency Test," *Journal of the Textile Institute Transactions*, vol. 36, p. T67, 1945.
- [35] D. Kim, D.-W. Lee, W. Choi, and J.-B. Lee, "A Super-Lyophobic 3-D PDMS Channel as a Novel Microfluidic Platform to Manipulate Oxidized Galinstan," *Journal of Microelectromechanical Systems*, vol. 22, p. 1267, 2013.
- [36] W. Choi, A. Tuteja, J. M. Mabry, R. E. Cohen, and G. H. McKinley, "A modified Cassie–Baxter relationship to explain contact angle hysteresis and anisotropy on non-wetting textured surfaces," *Journal of Colloid and Interface Science*, vol. 339, p. 208, 2009.
- [37] Y. Yoon, D.-W. Lee, J.-H. Ahn, J. Sohn, and J.-B. Lee, "One-step fabrication of optically transparent polydimethylsiloxane artificial lotus leaf film using under-exposed under-baked photoresist mold," in *Micro Electro Mechanical Systems (MEMS), 2012 IEEE 25th International Conference on*, 2012, p. 301.
- [38] D. Kim, D. Jung, J. H. Yoo, Y. Lee, W. Choi, G. S. Lee, *et al.*, "Stretchable and bendable carbon nanotube on PDMS super-lyophobic sheet for liquid metal manipulation," *Journal of Micromechanics and Microengineering*, vol. 24, p. 055018, 2014.
- [39] D. Jung, K. H. Lee, D. Kim, D. Burk, L. J. Overzet, and G. S. Lee, "Highly Conductive Flexible Multi-Walled Carbon Nanotube Sheet Films for Transparent Touch Screen," *Japanese Journal of Applied Physics*, vol. 52, p. 03BC03, 2013.
- [40] J. C. Lötters, W. Olthuis, P. H. Veltink, and P. Bergveld, "The mechanical properties of the rubber elastic polymer polydimethylsiloxane for sensor applications," *Journal of Micromechanics and Microengineering*, vol. 7, p. 145, 1997.

- [41] Y. Zhou, L. Hu, and G. Grüner, "A method of printing carbon nanotube thin films," *Applied Physics Letters*, vol. 88, p. 123109, 2006.
- [42] D. Kim and K.-S. Yun, "Patterning of carbon nanotube films on PDMS using SU-8 microstructures," *Microsystem Technologies*, vol. 19, p. 743, 2013.
- [43] D. Fuard, T. Tzvetkova-Chevolleau, S. Decossas, P. Tracqui, and P. Schiavone, "Optimization of poly-di-methyl-siloxane (PDMS) substrates for studying cellular adhesion and motility," *Microelectron. Eng.*, vol. 85, p. 1289, 2008.

IntechOpen

